Promoting enzyme catalysis via azobenzene facilitated vibrational energy transfer

Ranit Lahmy, ‡ [b] Caroline Hiefinger, ‡ [a] Fjoralba Zeqiri, ‡+ [b] Sabrina Mandl,[a] Kristina Straub,[a] Willibald Stockerl,[b] Ruth M. Gschwind,[b] Till Rudack,[a] Burkhard König,[b] and Andrea Hupfeld*[a]

AUTHOR ADDRESS [a] Institute of Biophysics and Physical Biochemistry and Regensburg Center for Biochemistry, University of Regensburg, Universitätsstraße 31, D-93053 Regensburg (Germany). [b] Institute of Organic Chemistry, University of Regensburg, Universitätsstraße 31, D-93053 Regensburg (Germany).

KEYWORDS. azobenzene • enzyme catalysis • protein dynamics • vibrational energy transfer • unnatural amino acids

ABSTRACT: Besides its capability to switch between two configurations, azobenzene converts light energy to vibrational energy (VE). Incorporation of the azobenzene-based unnatural amino acid AzoF can, hence, facilitate the transfer of VE into an enzyme. We were interested whether this VE transfer might increase conformational dynamics important for catalysis to ultimately promote enzyme activity. To this end, allosteric enzymes are well-suited model systems since allosteric regulation is mediated by conformational dynamics. To promote catalysis via VE transfer, we selected two positions for incorporation of AzoF in the prominent allosteric bi-enzyme complex imidazole glycerol phosphate synthase (ImGPS). While W123 in the HisH subunit is close to the critical active site and a key player for allostery, S55 in the HisF subunit is more distant contributing only moderately to allostery, as shown via in-depth biophysical and computational evaluations. We further demonstrated that simultaneous irradiation of AzoF with 365 nm and 420 nm produces higher amounts of VE than monochromatic irradiation and results in the appearance of a third spectroscopic signal originating from the azobenzene moiety. Remarkably, enzyme activity increased upon dichromatic irradiation for ImGPS(W123AzoF) but not for wild-type ImGPS or ImGPS(S55AzoF) and returned to initial activity values in the dark indicating that the change in activity was caused by VE transfer. Our findings provide a proof-of-concept for promoting enzyme activity by VE transfer and open up further possibilities to study the relationship between dynamics and enzyme catalysis.

INTRODUCTION

Photoswitches that isomerize between two configurational states upon light exposure are common control elements of protein activity in nature. They work by modulating the conformational flexibility of their protein target,[1–5] which is also a crucial component of catalysis in enzymes. In general, proteins comprise multiple conformational states, which are represented by local or global energy minima that are separated by energy barriers $\Delta G^{\ddagger}$ (**Figure 1A**).[6,7] Conformational flexibility is created by the exchange between these conformational states in a timely manner. The free energy value of the conformational states thereby defines the distribution between populations in equilibrium, whereas the size of the energy barrier determines the kinetics of the conformational state interconversions. We will refer to the exchange kinetics with the term "dynamics" from now on. While small barriers allow dynamics on the sub-microsecond timescale (≤µs), larger barriers reduce the rate to the >µs timescale. Isomerization of a photoswitch that is part of the protein can regulate protein activity either by stabilizing a highly active (global) conformational state ("A"), by increasing dynamics between an inactive ("I") and active (global) conformational state ($k_{I\rightarrow A}$) via reduction of $\Delta G^{\ddagger}_{I\rightarrow A}$, or by both (**Figure 1B**). This has been shown on the example of photoswitch-containing photoreceptors in the field of optogenetics.[1–5] A different approach to increase protein and specifically enzyme activity is to transmit energy into the protein, e.g. in the form of a temperature increase (ΔT). This global energy input does not change the conformational landscape. Instead, following the Arrhenius law, the gained energy is used to overcome $\Delta G^{\ddagger}_{I\rightarrow A}$ and increase the catalytically essential interconversion rate $k_{I\rightarrow A}$ (**Figure 1C**). In this study, we were interested whether a site-directed energy input could also promote protein dynamics and as a result enzyme catalysis. In our concept (**Figure 1D**), we intend to capture light-energy (cyan arrow) locally, which is then transmitted to the enzyme (black arrow) and used to overcome $\Delta G^{\ddagger}_{I\rightarrow A}$ thereby accelerating $k_{I\rightarrow A}$.

To this end, a molecular system (light grey molecule) is required that injects light energy into the enzyme in the form of vibrational energy (VE). This process is known as VE transfer (VET) and includes excitation of a so-called VET donor, which subsequently decays to the ground state via non-radiative internal conversion. The generated VE can spread through the enzyme provided that the decay happens on an ultrafast timescale, which produces sparsely localized low-frequency modes in the vicinity of the VET donor.[8–10] The photoswitch azobenzene, which interconverts between an *E* and *Z* configuration, has previously been shown to be such a VET donor.[9] The planar *E* isomer exhibits C_{2h} symmetry,[11,12] which allows a $\pi\rightarrow\pi^*$ transition with a strong light absorbance at ~320 nm and prohibits a $n\rightarrow\pi^*$ transition with only weak light-absorbance at ~450 nm (**Figure 1E**).[13] Irradiation with UV light close to the $\pi\rightarrow\pi^*$ transition (λ ~ 365 nm) results in S0→S2 excitation and subsequent photoisomerization of the *E* to the *Z* isomer. Due to the non-planar configuration

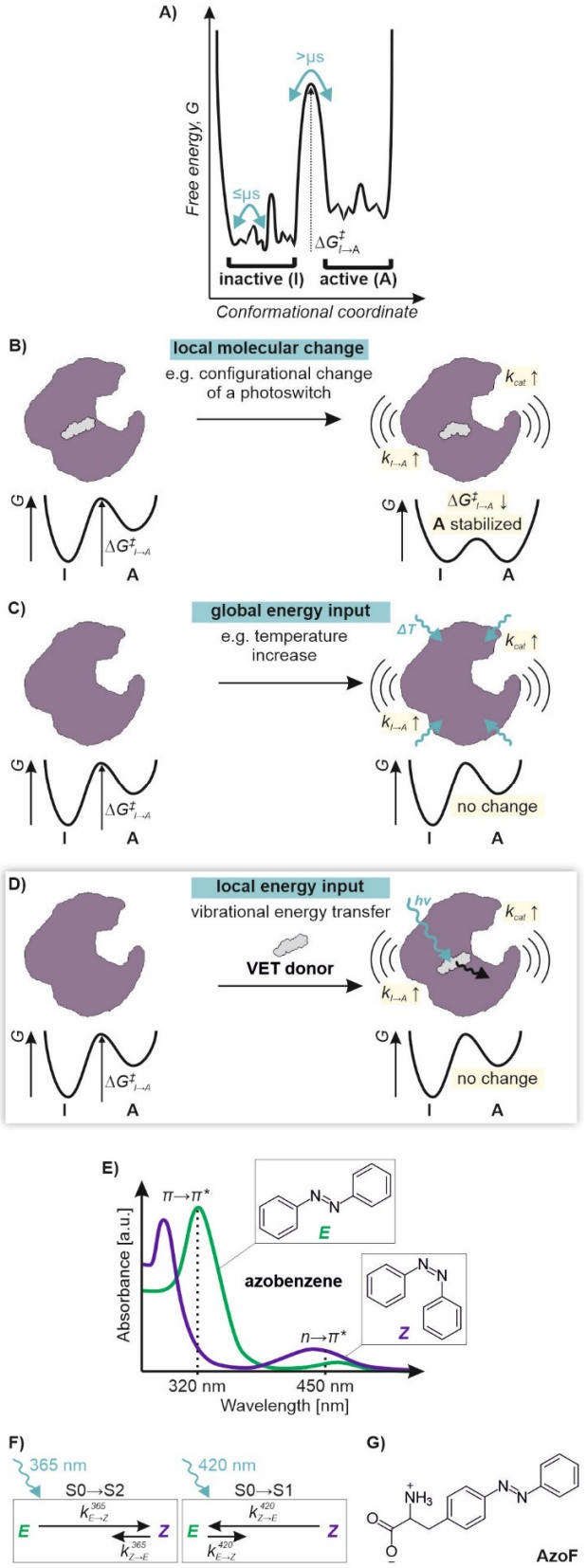

Figure 1. Concept to increase enzyme catalysis via VET. A) Exemplary two-dimensional cross-section through the three-dimensional energy landscape of a protein. Local minima represent the conformations and local maxima the energy barriers $\Delta G^{\ddagger}$ that define the rate (cyan) of the interconversion between conformations. Global conformations can exhibit different catalytic strengths in enzymes. B) A local molecular change, such as the configurational change of a photoswitch (grey), can increase the catalytic turnover k_{cat} through stabilization of an active conformation A and reduction of the energy barrier $\Delta G^{\ddagger}_{I\to A}$ between the inactive conformation I and A leading to an increase in dynamics $k_{I\to A}$. C) A global energy input such as a raise in temperature helps to overcome an existing energy barrier and enhances enzyme dynamics ($k_{I\to A}$) and catalysis (k_{cat}). D) Enzyme dynamics and catalysis might also be promoted by a local energy input. This can be realized by a VET donor associated to the enzyme, which collects light energy and injects it into the enzyme following a non-radiative decay. E) Azobenzene derivatives switch between two isomers, *E* and *Z*, which exhibit different absorbance spectra. F) Irradiation at either the $\pi\to\pi^*$ (λ ~365 nm) or the $n\to\pi^*$ (λ ~420 nm) transition leads to S0→S2 or S0→S1 excitation of both azobenzene isomers, respectively. *E*↔*Z* isomerization is thereby a photo-induced equilibrium reaction that establishes either a *Z*- or an *E*-enriched PSS. G) Azobenzene can be directly incorporated into ImGPS through attachment of an amino acid moiety in para position of the central C-N=N-C link generating AzoF.

with C_2 symmetry,[14,15] the $\pi\to\pi^*$ transition is weakened in *Z* leading to a decrease and a shift of the UV band to lower wavelengths, whereas the now allowed $n\to\pi^*$ transition causes a stronger signal at ~450 nm.[13] Irradiation with visible light close to the $n\to\pi^*$ transition (λ ~ 420 nm) results in S0→S1 excitation and subsequent back-isomerization of *Z* to *E*. The rates of photoisomerization, just like any other photo-induced reaction, thereby depend on ε^{λ} as the extinction coefficient giving the probability that a molecule is excited, and $\phi^{\lambda}_{E\to Z}$ and $\phi^{\lambda}_{Z\to E}$ as the quantum yield of the respective reaction representing the probability that the molecule isomerizes, as shown in **Equation 1**.

$$k^{\lambda}_{E\to Z} = \varepsilon^{\lambda}_{E} \times \phi^{\lambda}_{E\to Z};\ k^{\lambda}_{Z\to E} = \varepsilon^{\lambda}_{Z} \times \phi^{\lambda}_{Z\to E}$$

Equation 1

Since both isomers absorb light at 365 nm with different intensities ($\varepsilon^{365nm}_{E} \gg \varepsilon^{365nm}_{Z}$) and isomerize upon excitation with different quantum yields ($\phi^{365nm}_{E\to Z}$ ~ 0.16 and $\phi^{365nm}_{Z\to E}$ ~ 0.39)[16] a photo-induced equilibrium is established that favors the *Z* configuration (**Figure 1F**). This equilibrium is named photostationary state (PSS). Likewise, irradiation with 420 nm results in an *E*-enriched PSS again due to different absorbance intensities ($\varepsilon^{420nm}_{E} < \varepsilon^{420nm}_{Z}$) and quantum yields ($\phi^{420nm}_{E\to Z}$ ~ 0.29 and $\phi^{420nm}_{Z\to E}$ ~ 0.45)[16] at that wavelength. Importantly, the quantum yields are rather low indicating that most of the excited azobenzene molecules (~55–84% as estimated from the quantum yields) give off the obtained energy in an ultrafast (<ps to ps)[17] and non-radiative[17,18] S2→S0 or S1→S0 decay. The energy that is set free by this decay can be injected as VE. Notably, the amount of VE that is generated by azobenzene is defined by the energetic state (S1 or S2) of excitation, the extinction coefficient and the quantum yield. The three factors depend on the irradiation wavelength and on the *E*:*Z* ratio, which is in turn established by the irradiation wavelength.

We anticipated that the efficiency of VET will be highest when the azobenzene molecule is covalently linked to the enzyme. This can be achieved by attaching an amino acid moiety to the azobenzene creating the unnatural amino acid phenylalanine-4'-azobenzene (AzoF; **Figure 1G**).[19] Following the amber suppression technique, the

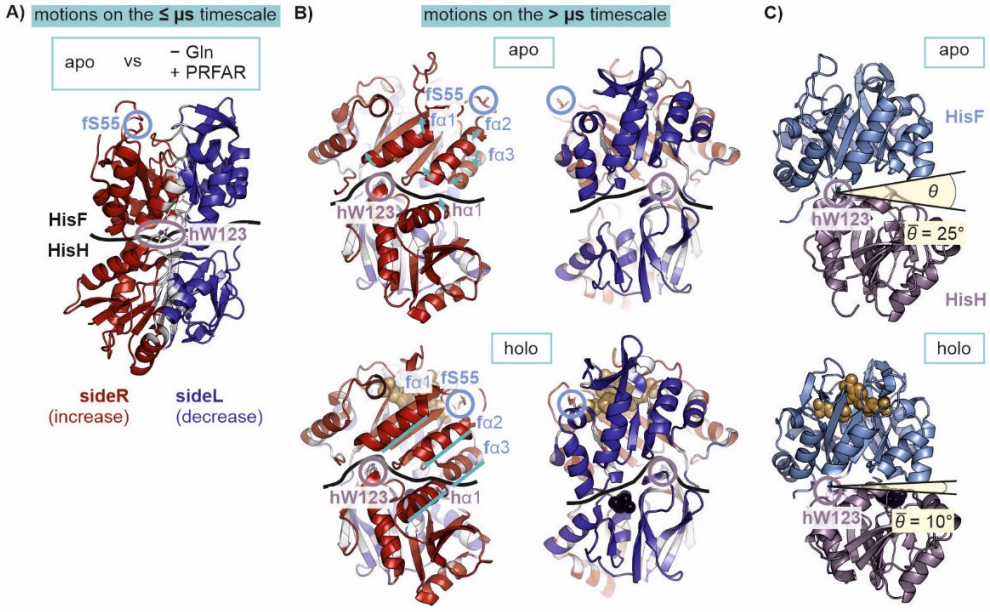

Figure 2. Conformational flexibility of the allosteric bi-enzyme complex ImGPS. A) Sectioning of ImGPS based on geometrical aspects separates computationally measured increase or decrease in correlated motions induced by binding of PRFAR to apo ImGPS. [20–23] Residues not part of sideR or sideL are assigned to the ambiguous side (white). B) In sideR, major conformational changes (depicted by cyan arrows and lines) upon formation of holo ImGPS occur (red) as determined in crystallographic snapshots (PDB-ID = 7ac8, chains CD and EF),[24] NMR experiments[24] as well as computational studies on the ms timescale.[25] In sideL (blue), the rearrangements are less pronounced and result from the interface closure. C) Representation of the interface closure of ImGPS upon binding of PRFAR and glutamine. The interface angles $\boldsymbol{\theta}$ were calculated in MD simulations from the α-carbons of fF120, hW123, and hG52; given is the mean interface angle $\bar{\boldsymbol{\theta}}$. Apo ImGPS complex: PDB-ID = 1gpw, chains CD; holo ImGPS: PDB-ID = 7ac8, chains EF. Note: The positions of AzoF incorporation, hW123 (dark violet) and fS55 (light blue) are highlighted.

incorporation site is marked by an amber codon in the genetic code of the enzyme and AzoF is co-translationally incorporated by using a heterologous, orthogonal aminoacyl-tRNA-synthetase/tRNA (aaRS/tRNA) pair.[26,27] AzoF is often used to engineer light-sensitive proteins, known as photoxenoproteins.[26,28] Recently, we have achieved to control enzyme activity by a factor of ~10-fold in the allosteric bi-enzyme complex imidazole glycerol phosphate synthase (ImGPS) using the configurational switch of AzoF.[29,30] ImGPS belongs to the family of glutamine amidotransferases consisting of a glutaminase subunit, HisH, and a cyclase subunit, HisF (**SI part1: Figure S1**).[31] HisH produces ammonia, which travels through an intermolecular channel to the active site of HisF where it is required for the cleavage of *N*′-[(5′-phosphoribulosyl)formimino]-5-aminoimidazole-4-carboxamide ribonucleotide (PRFAR). Notably, binding of PRFAR[32] or its metabolic precursor *N*′-[(5′-phosphoribosyl)formimino]-5-aminoimidazole-4-carboxamide ribonucleotide (ProFAR) to HisF induces an allosteric stimulation of HisH that results in a drastic increase of glutamine hydrolysis.[29]

ImGPS is one of the best model systems to study the effect of conformational flexibility on catalysis. Crystal structures of the apo and glutamine bound complex showed early on that the active site of HisH is lacking the catalytically important oxyanion hole, which is present in other glutamine amidotransferases.[31,33] Studies throughout the last decade have shown that the stabilization of an active ("A") oxyanion hole conformation is one part of multiple changes in the conformational flexibility of ImGPS.[21–25,29,31,34,35]. Initial computational studies thereby focused on the role of PRFAR as an allosteric activator, comparing PRFAR bound ImGPS to apo ImGPS on the ≤µs timescale and analyzing the variance by means of eigenvectors.[20–23] The detected changes clustered into two regions in ImGPS (**Figure 2A**). In sideR (red) the correlated motions increased upon PRFAR binding, whereas in sideL (blue) the correlated motions decreased. In agreement, subsequent NMR results showed that residue motions on the millisecond timescale (>µs) also occur mainly in sideR after binding of PRFAR to ImGPS.[34] Recent reports have now demonstrated that both PRFAR (or ProFAR) and glutamine are required to stabilize an active oxyanion hole conformation and, hence, activate HisH allosterically (**SI part1: Figure S2A**).[24,25] The global conformational transitions that accompany this change mainly take place in sideR of ImGPS (**Figure 2B**, red).[24] In particular, α-helices fα1 (f delineates motifs in HisF), fα2, fα3, and hα1 (h delineates motifs in HisH) shift and rotate (cyan arrows) until all four helices are parallel to each other (cyan lines). Further conformational rearrangements occur in sideL (blue), however they are only minimal in comparison and are mainly associated with a closure of the interface. Notably, the interface itself is not static but fluctuates around a mean angle $\bar{\theta}$ in a so-called "breathing" motion using the cation-π interaction of the two residues fR249 and hW123 as an anchor. Binding of both PRFAR and glutamine reduces the mean angle $\bar{\theta}$ to ~10° in holo ImGPS,[24,25] compared to ~25° in apo ImGPS (**Figure 2C**).[31] Ultimately, accelerated molecular dynamics (MD) simulations could show that PRFAR and glutamine binding not only cause the stabilization of the active oxyanion hole conformation but also reduce $\Delta G^{\ddagger}_{I\to A}$ and increase the dynamics (**SI part1: Figure S2B**). Another study simultaneously demonstrated that the energy barriers for the chemical step of glutamine hydrolysis are also reduced by allosteric stimulation.[36]

Within this study we focus on the proof-of-concept of promoting enzyme catalysis through VET. For this purpose, ImGPS is a very well-suited model system owing to the comprehensive knowledge on its allostery- and catalysis-involved dynamics. To this end, we first characterized two previously identified positions in ImGPS to assess whether the energy that is injected by an incorporated AzoF at these positions might be effectively transferred to the active site of HisH where it might support catalytically important interconversions. We

then tuned the irradiation conditions to facilitate different amounts of VE in the AzoF-containing ImGPS variants, and subsequently measured the effects on the turnover rate. Finally, we could show that enzyme activity of one ImGPS variant was promoted by dichromatic irradiation and that it was recovered to initial activity levels after returning to the dark state.

RESULTS AND DISCUSSION

Evaluation of position hW123 and fS55 for VE injection

Amber suppression facilitated incorporation of AzoF allows us to inject VE site-specifically within ImGPS. However, we contemplated that various factors might influence the effective activation of catalysis via VET. First and foremost, we considered that the position of AzoF incorporation should be involved in allosteric events of ImGPS so that injected VE can support the allosterically relevant dynamics at this site or travel along an allosteric path. In our previous studies, we achieved to control HisH activity by 10-fold via introduction of AzoF at positions hW123 and fS55.[29,30] This allowed us to not only photocontrol enzyme activity but also allostery in ImGPS through the light-induced configurational change of the azobenzene. Initial structural, computational and biochemical studies proposed that the light-induced isomerization of AzoF might influence the conformational flexibility of ImGPS.[29,30] We therefore reasoned that both positions are also good starting points for promoting enzyme activity via VET. To validate hW123 and fS55 for our proof-of-concept, we characterized both positions considering three criteria: i) their involvement in specific allosteric activation events of HisH, ii) the changes introduced by AzoF incorporation, and iii) their distance to the oxyanion hole as a marker for the active site (**Table 1**).

We started by determining the role of hW123 and fS55 in specific allosteric events of ImGPS. For this, we first looked at the ≤μs motions associated with PRFAR binding to ImGPS that were already available from studies[20–23] that analyzed the variance by means of eigenvectors (**Figure 2A**). While hW123 is part of a region where motions remained unchanged, fS55 is part of sideR, which showed an increase of motions after PRFAR binding. Since PRFAR alone cannot facilitate the formation of the active conformation of ImGPS, we were further interested in the contribution of both positions to ≤μs motions induced upon PRFAR and glutamine binding in holo ImGPS. To this end, we performed molecular dynamics (MD) simulations based on the recently determined crystal structure of the holo complex[24] and compared it to the apo state (**SI part2: Figure S22**). We then analyzed the variance of each residue by means of a principal component analysis (PCA) that also works with eigenvectors. However, the detected changes did not cluster into specific regions with increased or decreased correlated motions that could be assigned to sideR and sideL (**SI part2: Figures S23–S25**). Instead, HisF remained largely flexible, while the interface and the HisH subunit, particularly its active site, were stabilized. Conclusively, hW123 stayed rigid, whereas fS55 kept its high flexibility.

Besides ≤μs motions, we analyzed the contribution of both positions in the allosterically essential interface closure that takes place on the >μs timescale. For this, we compared the crystal structures of apo and holo ImGPS[24,31] (**Figure 2B,C**). While hW123 is crucial for the interface closure due to its function as a hinge residue, fS55 is part of loop2 that approaches the active site of HisF concomitant to the larger α-helical rearrangements after PRFAR binding but remains far from the complex interface.

In addition to the direct involvement in ≤μs and >μs conformational changes, hW123 and fS55 might be part of the allosteric signal transmittance from the HisF to the HisH active site. In the last decades, several computational studies have presented different allosteric pathways. However, only one of them used the fully activated holo ImGPS.[25] By performing shortest path map (SPM) analysis, they identified a network of residues that are important for the allosteric activation in six different states of the activation process. We have summarized the contribution of each identified residue to the six states (**SI part1: Figure S3**) and marked the respective positions by a sphere in the ImGPS complex in **Figure 3A**. The sphere size and color thereby indicate whether the residue is important for only one (smallest size, light cyan) or up to all six (increasing size, cyan to dark blue) states of the activation process. While hW123 is one of the key players for the allosteric activation, fS55 is not part of this computational allosteric pathway (white sphere). In agreement with the shortest path map study, contact analysis of our MD simulations showed that hW123 is highly connected within apo and holo ImGPS, whereas fS55 has only a few contacts within apo and holo ImGPS including PRFAR (**SI part2: Figure S26–S29**).

Table 1. Characterization of positions hW123 and fS55 regarding three different factors relevant for VET.

Involvement in allosteric events	hW123	fS55	Shown in
Contribution to ≤μs motions associated to PRFAR binding[20–23]	×	✓	Figure2A
Contribution to the HisF-HisH interface closure[24,25]	✓	×	Figure2B,C
Part of a computationally determined allosteric pathway[25]	✓	×	Figure 3A, SI part1: Figure S3
Part of an experimentally determined allosteric pathway	—[a]	✓	Figure 3B, SI part1: Figure S4
Changes after incorporation of AzoF			
Increase of unstimulated HisH activity[29]	✓	×	Table 2
Increase of conformational flexibility in ImGPS[29]	✓	×	Figure 3C
VET distance to the oxyanion hole (hV51 amide)			
Apo ImGPS	16.0 Å	32.9 Å	SI part1: Figure S6
Holo ImGPS	15.8 Å	26.5 Å	SI part1: Figure S6

[a] Note that hW123 was not mutated to alanine in this experimental set up, because of its key role in complex formation.

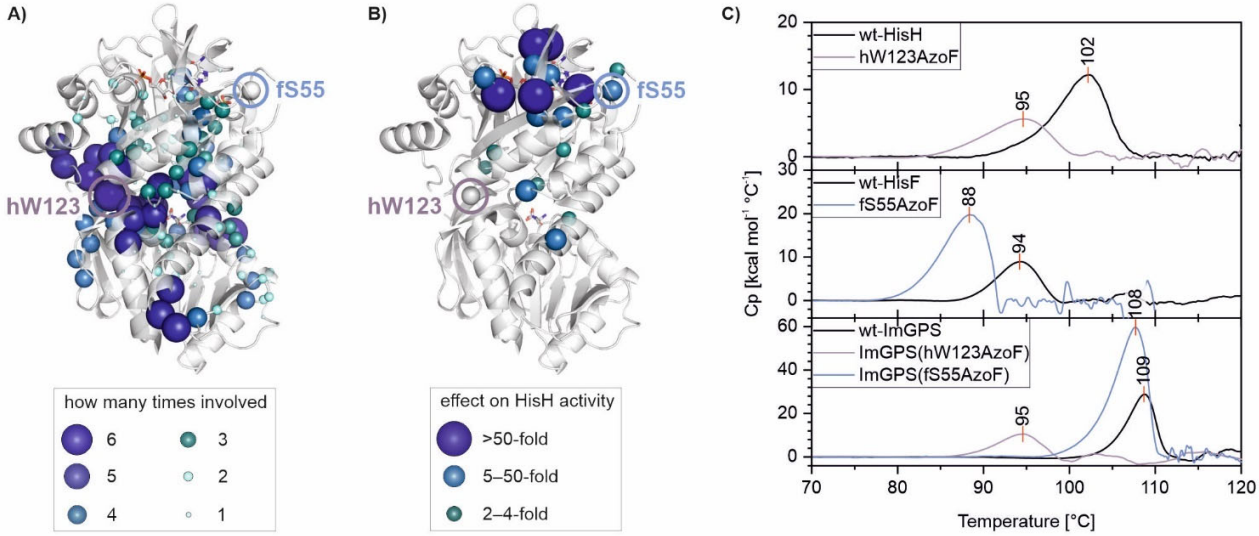

Figure 3. Characterization of positions hW123 and fS55 regarding their involvement in allosteric events and changes after incorporation of AzoF. A) Computationally determined allosteric pathway summarizing previously reported SPM results.[25] Colored spheres indicate how many times the residues are involved in the six states of the allosteric activation process. For details see **Figure S3**. B) Experimentally determined allosteric pathway summarizing the results of an alanine screen. Colored spheres indicate to what degree HisH activity was hampered by mutation of the respective residue to alanine. For details see **Figure S4**. C) Differential scanning calorimetry measurements comparing HisH, HisF and ImGPS variants. Reaction conditions: 20 µM protein, 50 mM HEPES (pH 7.5), 100 mM NaCl. Data for wt-HisH, hW123AzoF, wt-ImGPS, and ImGPS(hW123AzoF) were adapted from ref[29].

We further complemented these computational data with an experimental analysis of an allosteric activation path in ImGPS. For this purpose, we identified all residues that changed their side chain conformation in a comparison of the apo and holo X-ray structures of the ImGPS complex. We then mutated these positions to alanine, determined the HisH activity in the presence of an excess of ProFAR, and plotted the resulting apparent k_{cat} values ($k_{cat,app}$) in a bar graph (**SI part1: Figure S4**). In 20 variants, HisH activity was hampered to various degrees, which is visualized in **Figure 3B**. The sphere size and color thereby indicate whether the effect of the mutated residue on HisH activity is weak (2–4-fold; smallest size, cyan), medium-strong (5–50-fold; medium size, blue) or strong (>50-fold; largest size, dark blue). While hW123 (white sphere) was not part of this alanine screen because we considered it crucial for proper complex formation, mutation of fS55 reduced HisH activity 5-fold.

Next, we compared the influence of AzoF-incorporation at positions hW123 and fS55 on allostery and its associated dynamics. Our previous studies revealed that the HisH activity in absence of an allosteric ligand of ImGPS(hW123AzoF) is increased by 20-fold to ~181×10^{-3} min^{-1} compared to ~9×10^{-3} min^{-1} in wt-ImGPS (**Table 2**).[29] We considered this a strong indication that the conformational flexibility of the bi-enzyme complex is altered in the ImGPS(hW123AzoF) variant, which was supported by thermal stability measurements using differential scanning calorimetry (**Figure 3C**).[29] The denaturation midpoint of ImGPS(hW123AzoF) was reduced to 95°C compared to 109°C of wt-ImGPS, suggesting that ImGPS(hW123AzoF) comprises more loose interactions and, hence, an increased flexibility compared to wt-ImGPS. Next, we determined HisH activity in steady-state kinetics and thermal stability in differential scanning calorimetry for ImGPS(fS55AzoF). However, k_{cat} was found to be similar to the k_{cat} of wt-ImGPS (~9×10^{-3} min^{-1}) (**Table 2**; **SI part1: Figure S5**) and the denaturation midpoint of 108°C was comparable to the one of wt-ImGPS (**Figure 3C**). Hence, AzoF incorporation at position fS55 appeared to have little influence on the conformational flexibility of ImGPS.

Table 2. Steady-state kinetics of wt-ImGPS, ImGPS(hW123AzoF) and ImGPS(fS55AzoF).

Variant	k_{cat} dark [min^{-1}]	k_{cat} 365 nm [min^{-1}]	LRF[d]
In the absence of an allosteric ligand[a]			
wt-ImGPS[29]	(9.3 ± 0.2) ×10^{-3}		
ImGPS(hW123AzoF)[29]	(181 ± 6) ×10^{-3}		
ImGPS(fS55AzoF)[b]	(8.6 ± 0.3) ×10^{-3}		
In the presence of PRFAR as allosteric ligand[c]			
wt-ImGPS[29,30]	41.4 ± 1.1	—	—
ImGPS(hW123AzoF)[29]	13.8 ± 1.4	26.2 ± 1.8	1.9 ± 0.1 ↑
ImGPS(fS55AzoF)[30]	6.0 ± 0.2	2.6 ± 0.2	2.3 ± 0.2 ↓

[a] HisH activity: 20 mM Tris-HCl (pH 7.0), 20 mU/mL GOX, 0.15 g/L HRP, 1 mM 4-aminoantipyrine, 1 mM phenol, 0.1–80 mM glutamine, and 10–25 µM ImGPS at 25°C. [b] This work. [c] ImGPS activity: 50 mM Tris-acetate (pH 8.5), 0.6 µM HisA (to convert ProFAR to PRFAR), 40 µM (saturated) ProFAR, 0.01–10 mM glutamine, and 0.1–0.2 mM ImGPS at 25°C. [d] The activity change is indicated by an upwards (activity increase) or downwards arrow (activity decrease). Note: values are given as mean ± standard error of mean (S.E.M.).

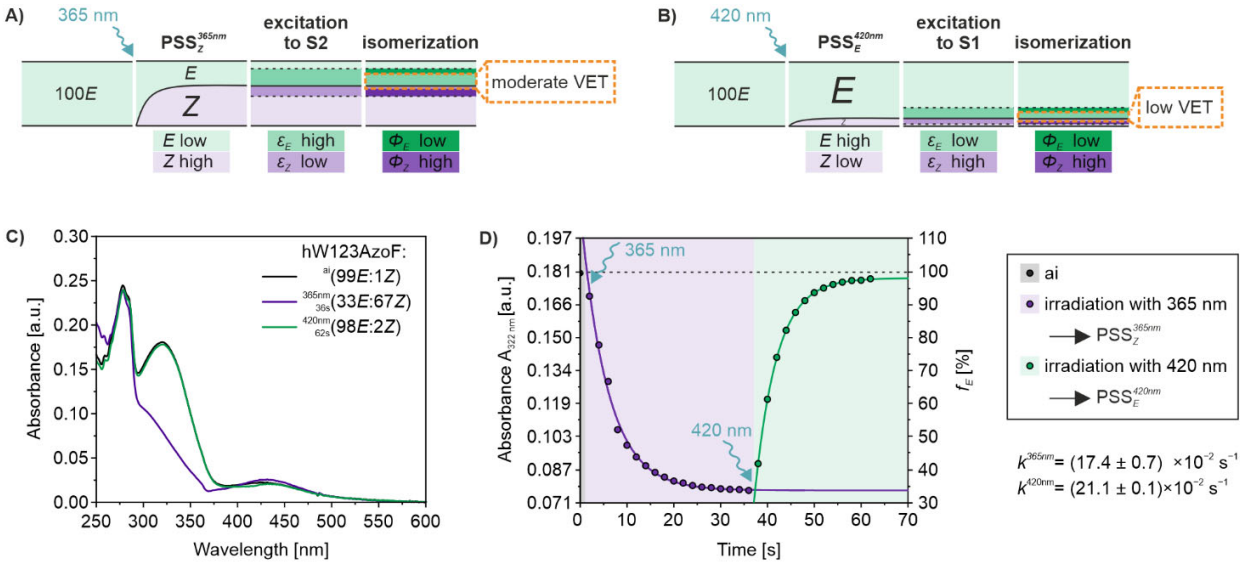

Figure 4. Establishment of moderate and low VET via monochromatic constantly powered irradiation. A,B) Illustration to explain the generation of moderate and low amounts of VE from 365 nm (A) and 420 nm (B) irradiation. Step 1: monochromatic irradiation establishes a PSS with different *E*:*Z* ratios. Step 2: extinction coefficients ε define the fraction of each isomer that is excited. Step 3: quantum yields ϕ determine the fraction of each isomer that isomerizes. Orange box: the residual fraction of each excited isomer decays radiationless to S0 giving off VE. C) UV/Vis spectra of 15 µM hW123AzoF (in 50 mM HEPES pH 7.5, 100 mM NaCl) in its as-isolated state (ai, black), in PSS_Z^{365nm} (violet) after 36 s of irradiation, and in PSS_E^{420nm} (green) after 62 s of irradiation (cf. D). D) Progress curve following the change of the approximate *E* isomer fraction (f_E) at 322 nm during 365 nm and subsequent 420 nm irradiation. See **SI part1: Figure S10** for a description of the approximation of f_E. Mono-exponential fitting of each section obtained the rate constants k^{365nm} and k^{420nm} ± standard error of fit (S.E.).

Finally, we considered that the vibrational energy that is injected by AzoF might only travel a limited range. Hence, we measured the distance of the Cα atoms of hW123 and fS55 to the amide nitrogen of hV51, which forms part of the oxyanion hole in the active site (**Figure S6**). Position hW123 is moderately close to the active site with distances of ~16.0 Å and 15.8 Å for apo and holo ImGPS, whereas position fS55 is comparably far away from the active site with distances of ~32.9 Å and 26.5 Å, respectively.

Taken together, the position hW123 appeared to be a key player for allostery in ImGPS. While its side chain conformation does not change during the rearrangement induced upon ligand binding, it steers the HisF-HisH interface closure as part of the hinge, is highly connected within the interface and as such is crucial for all six steps in the activation process. Moreover, incorporation of AzoF in this position, which is within a 17 Å distance to the active site, increased the flexibility of the complex. All these factors imply that ImGPS(hW123AzoF) is susceptible for VET induced activation of catalysis. In comparison, the position fS55 appears to be only moderately suitable for VET due to its large distance to the HisH active site and its marginal importance for allostery, highlighted by its low connectivity to other residues and its small contribution to an experimentally determined allosteric path. Nevertheless, since we could substantiate the contribution of both positions to allostery in ImGPS, we decided to test both variants in our subsequent experiments.

Establishment of moderate and low VET via monochromatic irradiation

The energy barrier of the chemical step in PRFAR-stimulated HisH is ~19 kcal mol^{-1}.[36] At present, it is difficult to predict how much VE needs to be injected into ImGPS to help overcome this barrier and promote enzyme catalysis. For this reason, we decided to use AzoF as VET donor, for which we can tune the amount of injected VE by the irradiation wavelength. To create high amounts of VE, we require a high extinction coefficient ε to increase the amount of excitation, a low quantum yield of isomerization ϕ to raise the amount of non-radiative and isomerization-less decay, and excitation into the high energetic S2 state. Irradiation of the *E* isomer with 365 nm meets all these criteria; however, it also generates a *Z*-enriched isomer equilibrium, which reduces the amount of VE due to a low ε and a high ϕ at this wavelength (**Figure 4A**). Accordingly, this state of equilibrium, which we dubbed PSS_Z^{365nm}, facilitates injection of moderate VE during 365 nm irradiation. In comparison, 420 nm irradiation facilitates an *E*-enriched equilibrium but here ε is generally low and excitation only reaches the S1 state. Consequently, we only expect low amounts of VE for irradiation with this wavelength and named the respective equilibrium PSS_E^{420nm} (**Figure 4B**). To substantiate this reasoning, we determined the *E*:*Z* ratios at PSS_Z^{365nm} and PSS_E^{420nm} of the monomeric hW123AzoF and fS55AzoF.

For this, we measured absorbance spectra in the ultraviolet to visible (UV/Vis) range before, during and after irradiation. We thereby used two light-emitting diodes (LEDs) with emission maxima of 365 nm and 420 nm, respectively, that were powered by a constant current ("constantly powered irradiation"). Thus, the sample is continuously exposed to light, which loses intensity over time (**SI part1: Figure S7A,B**). The UV/Vis spectra of the as-isolated hW123AzoF (**Figure 4C**, black) and fS55AzoF (**SI part1: Figure S8A**, black) before irradiation show a pronounced peak at ~280 nm, to which mainly the enzyme environment contributes, and two distinctive peaks at ~322 nm and ~425 nm representing the $\pi \rightarrow \pi^*$ and $n \rightarrow \pi^*$ transition of AzoF, respectively.

Next, we measured time-resolved UV/Vis spectra during 365 nm and subsequent 420 nm irradiation (**SI part1: Figure S8B,C; Figure S9**). By plotting the absorbance at 322 nm against time we visualized the establishment of the photo-induced *Z*-enriched and *E*-enriched equilibria and determined the overall rates of isomerization k^{365nm} and k^{420nm} using a mono-exponential function as justified elsewhere.[37] For hW123AzoF (**Figure 4D**), both PSS_Z^{365nm} and PSS_E^{420nm} were established after 20–30 s with k^{365nm} ~ 17.4×10^{-2} s^{-1} and k^{420nm} ~ 21.1×10^{-2} s^{-1}, and half-times of $t_{½(365nm)}$ ~ 4.0 s and $t_{½(420nm)}$ ~ 3.3 s, respectively. Irradiation of fS55AzoF (**SI part1: Figure S8D**) was similarly fast with k^{365nm} ~ 21.0×10^{-2} s^{-1} and k^{420nm} ~ 25.6×10^{-2} s^{-1}, and half-times of $t_{½(365nm)}$ ~ 3.3 s and $t_{½(420nm)}$ ~ 2.7 s, respectively.

We further estimated the *E*:*Z* ratios by peak deconvolution with Gaussian functions as described in detail in the supplement (**SI part1: Figure S10**).[38–40] As a result, we obtained *E*:*Z* ratios at PSS^{365nm} of 33*E*:67*Z* for hW123AzoF and 32*E*:68*Z* for fS55AzoF, and at PSS^{420nm} of 98*E*:2*Z* for hW123AzoF and 100*E*:0*Z* for fS55AzoF (**Figure 4C**; **SI part1: Figure S8A**). Note that our estimation relies on the assumption that the as-isolated protein is thermally equilibrated to 100*E*:0*Z*. However, minimal exposure to light during the handling of the samples can easily disrupt the thermal equilibrium and change the *E*:*Z* ratio introducing a bias into the approach. More quantitative ways of estimation such as high-performance liquid chromatography as used for isolated AzoF,[41] or spectrophotometric determination techniques as used for photoreceptors[42] are not viable for AzoF-containing proteins; for the latter this is due to the completely overlapping absorbance spectra of *E* and *Z*. Hence, slight deviations in *E*:*Z* ratios at the PSS, when compared to other studies,[29,30,41] might be traced back to this bias.

In conclusion, our findings confirm that 365 nm and 420 nm irradiation produce a *Z*-enriched and *E*-enriched equilibrium, respectively, and further emphasize that these monochromatic irradiation setups limit the intensity of VE that can be injected.

Establishment of high VET via dichromatic irradiation

We concluded that the amount of VE might be increased by maximizing the *E* isomer fraction (f_E) in the photo-induced equilibrium during irradiation at the $\pi \rightarrow \pi^*$ transition. While this might be possible via tuning the irradiation wavelength, this approach also changes the extinction coefficients and quantum yields of isomerization, which might again reduce VET. Instead, we contemplated that simultaneous irradiation at the $\pi \rightarrow \pi^*$ and $n \rightarrow \pi^*$ transition might boost the back-reaction of the *Z* isomer and result in a higher f_E at the PSS without changing the extinction coefficients or quantum yields. Owing to the parallel irradiation at 365 nm and 420 nm, the amounts of VE produced by either S2 or S1 excitation are combined generating high VE intensities (**Figure 5A**). Accordingly, we named this theoretical *E*-enriched state of equilibrium $PSS_E^{365/420nm}$.

To test our hypothesis that f_E can be increased upon dichromatic irradiation, we used the same LEDs as for monochromatic irradiation with emission maxima at 365 nm and 420 nm. This time, however, we powered the LEDs using pulse-width-modulation ("pulsed irradiation"), by which the sample is exposed to light pulses of consistent intensity (**SI part1: Figure S7C**). Since the emission spectra of the LEDs were unchanged, monochromatic pulsed irradiation obtained the same *E*:*Z* ratios at PSS_Z^{365nm} and PSS_E^{420nm} than with constantly powered irradiation (cf. **Figure 4C** and **Figure 5B**). Moreover, to decrease the temperature output during irradiation, we realized dichromatic irradiation by using alternating instead of two parallel 365 nm and 420 nm pulses (**SI part1: Figure S7D**).

We measured time-resolved UV/Vis spectra for hW123AzoF during irradiation with various pulse frequencies to evaluate whether an *E*-enriched equilibrium was established. Since the rates of isomerization are <1 s^{-1} (**Figure 4D**), we chose 1, 10, 100 and 1000 Hz (**Figure 5C**; **SI part1: Figure S11A–D**). Notably, the absorbance for 1 Hz irradiation alternated between higher and lower absorbance values with a $\Delta A_{322\,nm}$ of ~0.003 a.u. indicating that a fraction of AzoF switched back and forth in response to the alternating 365 nm and 420 nm irradiation. To estimate the percentage of AzoF that switched with each cycle, we compared the spectra to a cycle performance of hW123AzoF, in which AzoF was switched 31 times from PSS_Z^{365nm} to PSS_E^{420nm} and back resulting in a $\Delta A_{322\,nm}$ of ~0.098 a.u. (**SI part1: Figure S11E**). Comparison of both $\Delta A_{322\,nm}$ confirmed that the toggling of absorbance in the 1 Hz irradiation experiment was negligible. In the 10–1000 Hz irradiation experiments, the absorbance signals did not change over time. However, a drop in absorbance at 322 nm of ~0.033 a.u. compared to the absorbance of as-isolated hW123AzoF (**SI part1: Figure S11F**) indicated that a photo-induced equilibrium was reached prior to the start of our measurement.

To capture the establishment of the photo-induced equilibrium, we measured time-resolved UV/Vis spectra for hW123AzoF (**SI part1: Figure S12A**), for which we simultaneously started the measurements and the dichromatic pulses using 1000 Hz and followed the reaction for 20 min. By plotting the absorbance at 322 nm against time we could visualize the formation of a PSS for the dichromatic irradiation. Contrary to the monochromatic irradiation, the isomerization reaction of hW123AzoF did not follow a mono-exponential function (**Figure 5D**). Instead, an initial rapid decline of the signal was followed by a much slower increase. The presence of these two reaction phases indicated that the reaction might follow a double-exponential function, which we used to fit our data. The fit obtained excellent p-values for both rates below the 0.05 significance level, and good R^2 values. The first reaction occurred with a rate k_{1st} of ~45.4×10^{-2} s^{-1} and a half-time of ~1.5 s on the same timescale as the isomerization reactions induced by monochromatic irradiation. Accordingly, the first phase is concluded after <30 s, which is comparable to the monochromatic irradiation experiments (**Figure 5D** inset and **Figure 4D**). However, the second reaction was >500-fold slower with k_{2nd} of ~8.9×10^{-4} s^{-1} and a half-time of ~13.0 min. We also performed the same measurement for fS55AzoF (**SI part1: Figure S12B–D**), which followed the same general reaction course. However, the first phase was faster than for hW123AzoF, so that we were not able to fit our data with a double-exponential function. Mono-exponential fitting of the second reaction phase obtained an apparent k_{2nd} of ~14.8×10^{-4} s^{-1} with a half-time of ~7.8 min, which is similar to the k_{2nd} of hW123AzoF. As a result of the double-exponential behavior, the hW123AzoF and fS55AzoF exhibited *E*:*Z* ratios of 71*E*:29*Z* and 65*E*:35*Z* after the first phase ($PSS1_E^{365/420nm}$), and approached *E*:*Z* ratios of 75*E*:25*Z* and 73*E*:27*Z* in the second phase

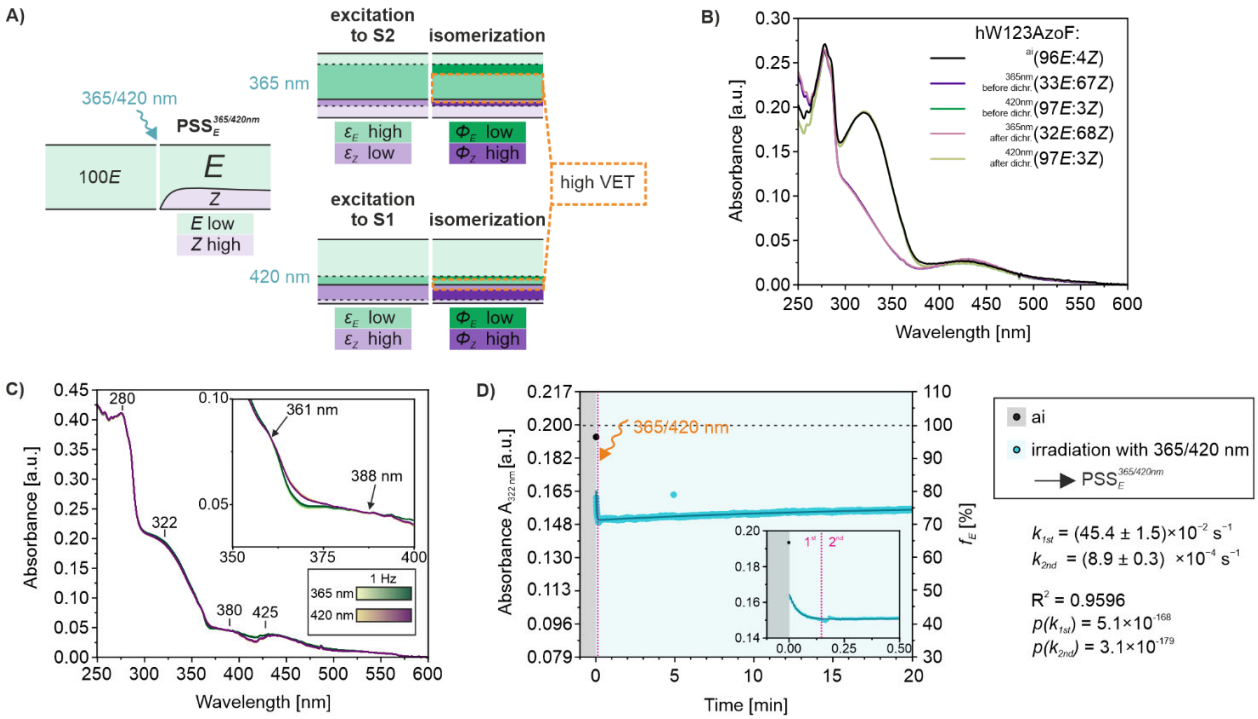

Figure 5. Establishment of high VET via dichromatic pulsed irradiation. A) Illustration to explain the generation of high amounts of VE from simultaneous 365 nm (top) and 420 nm (bottom) irradiation. Step 1: dichromatic irradiation establishes an *E*-enriched PSS. Step 2: extinction coefficients ε at the respective wavelength define the fraction of each isomer that is excited. Step 3: quantum yields ϕ at the respective wavelength determine the fraction of each isomer that isomerizes. Orange box: the residual fraction of each isomer decays radiationless to S0 giving off VE. B) UV/Vis spectra of hW123AzoF in its as-isolated state (ai, black), PSS_Z^{365nm} and PSS_E^{420nm}. The PSSs were obtained via monochromatic pulsed irradiation either before dichromatic pulsed irradiation ("dichr."; violet and green) or after dichromatic pulsed irradiation (pink and light-green). C) UV/Vis spectra of hW123AzoF acquired with a cycle time of 0.5 s during dichromatic irradiation with 1 Hz pulse frequency. Since we used alternating monochromatic pulses, every second spectrum corresponds to 365 nm or 420 nm irradiation as visualized with a green and violet gradient. The inset shows an additional isosbestic point of AzoF isomerization at ~361 nm (arrow) to the one at ~388 nm (cf. **SI part1: Figure 9**). D) Progress curve following the change of f_E at 322 nm during dichromatic irradiation with 1000 Hz pulse frequency. See **SI part1: Figure S10** for a description of the approximation of f_E. Double-exponential fitting obtained the rate constants for the first phase k_{1st} and for the second phase k_{2nd} ± S.E.

($PSS2_E^{365/420nm}$), respectively. Interestingly, $PSS2_E^{365/420nm}$ of both enzymes could again be converted to the *Z*-enriched PSSs and *E*-enriched PSSs with monochromatic irradiation (**Figure 5B**; **SI part1: Figure S12B**).

We therefore achieved our goal to increase f_E at the PSS ($f_{E,PSS}$) during 365 nm irradiation by simultaneous 420 nm irradiation. In general, $f_{E,PSS}$ depends on the *E*→*Z* and *Z*→*E* isomerization rates at the irradiation wavelengths, as shown for 365 nm irradiation in Equation 2[43]

$$f_{E,PSS} = \frac{[E]_\propto}{[E]_\propto + [Z]_\propto} = \frac{k_{Z\to E}^{365nm}}{k_{Z\to E}^{365nm} + k_{E\to Z}^{365nm}}$$

Equation 2

where $[E]_\propto$ and $[Z]_\propto$ are the equilibrium concentration of the *E* and *Z* isomers, respectively. For dichromatic irradiation we can deduce Equation 3

$$f_{E,PSS} = \frac{[E]_\propto}{[E]_\propto + [Z]_\propto} = \frac{k_{Z\to E}^{365nm} + k_{Z\to E}^{420nm}}{k_{Z\to E}^{365nm} + k_{Z\to E}^{420nm} + k_{E\to Z}^{365nm} + k_{E\to Z}^{420nm}}$$

Equation 3

in which $f_{E,PSS}$ depends on all reaction rates within the setup. In conclusion, only the extinction coefficients and quantum yields that define the reaction rates (Equation 1) determine $f_{E,PSS}$. Consequently, $f_{E,PSS}$ might be tuned by changing both factors. This can be done either by adapting the irradiation setup to e.g., an LED with a different emission spectrum, an LED with an emission maximum at a different wavelength or a monochromatic laser, or by introducing substituents on the azobenzene moiety of AzoF. Furthermore, it should be considered that various environmental factors influence both ε and ϕ, such as temperature, pH and salt concentration.[17] In this regard, the protein environment may also influence both factors and lead to variations in isomerization rates and *E*:*Z* ratios at different incorporation sites of AzoF. For hW123AzoF and fS55AzoF, we observed such variations though they were only moderate.

One important requirement for Equation 3 is that the isomerization reaction upon dichromatic irradiation is an equilibrium reaction as given in Equation 4.

$$E \underset{k_{Z\to E}^{365nm} + k_{Z\to E}^{420nm}}{\overset{k_{E\to Z}^{365nm} + k_{E\to Z}^{420nm}}{\rightleftharpoons}} Z$$

Equation 4

However, if this equilibrium reaction is the only reaction that takes place during dichromatic irradiation, we would expect a mono-exponential decay of the *E* isomer. The double-exponential shape of the progress curve therefore prompted us to further evaluate our data. We started this evaluation by comparing the rate constants that we obtained by monochromatic and dichromatic irradiation. For the isomerization reaction induced by monochromatic irradiation, the overall rate constants k^{365nm} and k^{420nm} of the photoisomerization reaction depend on the sum of the individual isomerization rates as shown for k^{365nm} in Equation 5.[37]

$$k^{365nm} = (k_{E\to Z}^{365nm} + k_{Z\to E}^{365nm}) d I_0^{365nm} F^{365nm}$$

Equation 5

where *d* is the path length of irradiation, I_0 is the intensity of the light source and *F* is the photokinetic factor, which depends on the absorbance at the irradiation wavelength. We assumed that this is also true for the isomerization reaction induced by dichromatic irradiation following Equation 6.

$$k^{365/420nm} = (k_{E\to Z}^{365nm} + k_{Z\to E}^{365nm}) d I_0^{365nm} F^{365nm} + (k_{E\to Z}^{420nm} + k_{Z\to E}^{420nm}) d I_0^{420nm} F^{420nm}$$

Equation 6

Consequently, $k^{365/420nm}$ should be almost equal to the sum of the two rates k^{365nm} and k^{420nm}. Looking at the first exponential phase of the hW123AzoF progress curve (**Figure 5D**), we found that its rate constant k_{1st} is with ~45.4×10^{-2} s^{-1} very similar to the sum of k^{365nm} and k^{420nm} of hW123AzoF obtained by monochromatic irradiation (~38.6×10^{-2} s^{-1}; cf. **Figure 4D**). We therefore assigned the initial rapid decline of the progress curve to the isomerization equilibrium between *E* and *Z*.

In the next step, we tried to identify the secondary reaction that took place upon dichromatic irradiation and that caused the double-exponential behavior. For this, we reanalyzed all time-resolved UV/Vis data (**SI part1 Figure S8–S12**) and found to our astonishment a fourth signal with an absorbance maximum at ~380 nm that only appeared during dichromatic irradiation alongside the protein signal (~280 nm), the $\pi\to\pi^*$ transition (~322 nm) and the $n\to\pi^*$ transition (~425 nm). This singal was particular noticeable in the UV/Vis trace of hW123AzoF during 1 Hz irradiation (**Figure 5C**). Because the absorbance alternated between higher and lower absorbance values, we could identify an additional isosbestic point for AzoF isomerization isomerization at ~361 nm during 1 Hz dichromatic irradiation compared to the two at ~278 nm and ~388 nm during monochromatic irradiation (**Figure 5C**; **SI part1: Figure S9**). This confirmed the existence of at least one other species in the reaction. Remarkably, termination of the dichromatic irradiation and subsequent monochromatic irradiation led to the disappearance of this additional UV/Vis signal (**Figure 5B**). This finding indicated that the unknown species is derived from *E* or *Z* AzoF and reacts back to either isomer. Hence, we suspect that the signal originates from an isomerization intermediate. However, we are uncertain of the type of transition this intermediate undergoes and why it only occurs during dichromatic irradiation. Furthermore, we cannot anticipate its contribution to VET. Given that all reaction intermediates of the *E*→*Z* and *Z*→*E* isomerization are energetically higher than S0,[44,45] excitation of this species might reach an Sn state. Interestingly, a previous study reported on the possibility that azobenzene is excited to Sn states upon dichromatic irradiation following a two-photon absorption process.[46] Decay back to S1 or S0 might then include both a non-radiative release of VE and a reaction to *E* or *Z*. We consider the photo-induced reaction to the *E* or *Z* isomers a viable possibility, because it explains the slow increase of the f_E in **Figure 5D**. As a consequence, $f_{E,PSS}$ will also depend on the reaction rates of this additional secondary reaction. Detailed experimental and computational data will be necessary to identify this species and analyze this phenomenon.

Finally, we aimed to measure the injection of VE into ImGPS upon monochromatic and dichromatic irradiation via NMR. However, we encountered technical limitations of the irradiation setup that we developed for the online irradiation of NMR samples (**SI part1: Figure S13–Figure S20**).[47] As a result, the isomerization rates were significantly slower than in our UV/Vis setup and we were not able to establish an *E*-enriched PSS, meaning that the NMR data were not comparable to the UV/Vis data. We therefore continued with a kinetic analysis aiming to confirm VET indirectly through promotion of enzyme activity.

Comparison of moderate and low VET effects with *E*↔*Z* switching effects on ImGPS activity

To determine the influence of VET on enzyme activity, we decided to follow the full ImGPS reaction (glutamine + PRFAR → glutamate + ImGP + AICAR; cf. **Figure S1**), which can be detected spectrophotometrically by following the signal of PRFAR at 300 nm (**Figure 6**). Since PRFAR turnover in HisF is rate-limited by the glutamine turnover in HisH, this reaction can be regarded as a measure of the PRFAR-stimulated HisH activity.[29] Our previous findings have shown that the photocontrol efficiency facilitated by *E*→*Z* switching in ImGPS(hW123AzoF) and ImGPS(fS55AzoF) is higher for the ProFAR-stimulated HisH activity than for the full ImGPS activity.[29,30] However, PRFAR is a stronger allosteric activator than ProFAR, meaning that the energy barriers in the chemical step of HisH are probably lower and might be overcome more easily by VET.

In preparation for the VET experiments, we measured the $k_{cat,app}$ values for the as-isolated ImGPS(hW123AzoF), ImGPS(fS55AzoF) and wt-ImGPS as a control. The obtained values at pH 7.5 of ~24.9 ± 1.2 min^{-1}, ~8.5 ± 0.4 min^{-1} and ~67.3 ± 6.0 min^{-1}, respectively, are slightly higher than those reported previously at pH 8.5 (**Table 2**) owing to the pH optimum at ~ pH 7.0.[30] We then set up our experiments to detect the change in rate caused by irradiation directly during turnover (cf. **Figure 6** and **Figure 7**).[26] For this, we initiated the reaction by the addition of ImGPS, followed the decrease of PRFAR turnover in the dark for ~5 min and then started the irradiation while following PRFAR turnover until the reaction stopped. This allowed us to detect effects that are primarily caused by the injection of VE at PSS_Z^{365nm}, PSS_E^{420nm} or $PSS1_E^{365/420nm}$, as these states were reached after a maximum of 20 s (cf. **Figure 4** and **Figure 5**). Furthermore, we use the term light-regulation factor (LRF) that compares the activity during irradiation with the activity in the dark. Finally, we performed the experiments with technical replicates, meaning more than one measurement with the same enzyme sample, and with biological replicates, meaning measurements with separately produced enzyme samples.

Table 3. ImGPS activities subjected to monochromatic irradiation.

Wavelength	Variant	$k_{cat,app}(dark)$ [min^{-1}]	$k_{cat,app}(during\ hv)$ [min^{-1}]	$k_{cat,app}(after\ hv)$ [min^{-1}]	LRF[a]	Replicates
During irradiation						
365 nm	ImGPS(hW123AzoF)	23.0 ± 2.2	42.4 ± 5.9	—	1.86 ± 0.23 ↑	4
	ImGPS(fS55AzoF)	11.8 ± 2.3	7.0 ± 1.3	—	1.68 ± 0.02 ↓	3
	wt-ImGPS	53.6 ± 5.9	52.8 ± 5.2	—	1.01 ± 0.02 ↓	3
420 nm	ImGPS(hW123AzoF)	24.1 ± 3.4	23.8 ± 3.1	—	1.01 ± 0.03 ↓	3
	ImGPS(fS55AzoF)	12.3 ± 1.4	14.3 ± 1.5	—	1.17 ± 0.07 ↑	6
	wt-ImGPS	53.3 ± 1.9	53.0 ± 3.5	—	1.01 ± 0.04 ↓	3
After 30 s irradiation						
365 nm	ImGPS(hW123AzoF)	23.3 ± 2.2	—	37.2 ± 4.6	1.60 ± 0.08 ↑[b]	4
420 nm			—	20.3 ± 1.5	1.83 ± 0.18 ↓[c]	
365 nm	ImGPS(fS55AzoF)	13.9 ± 1.3	—	9.5 ± 1.3	1.47 ± 0.06 ↓[b]	4
420 nm			—	15.6 ± 2.3	1.63 ± 0.12 ↑[c]	

ImGPS activity: 50 mM Tris-acetate (pH 7.5), 0.6 µM HisA (to convert ProFAR to PRFAR), ~40 µM (saturated) ProFAR, 10 mM (saturated) glutamine, and 0.025–0.2 mM ImGPS at rt. [a] The activity change is indicated by an upwards (activity increase) or downwards arrow (activity decrease). [b] LRF compares $k_{cat,app}(dark)$ and $k_{cat,app}(365\ nm)$. [c] LRF compares $k_{cat,app}(365\ nm)$ and $k_{cat,app}(420\ nm)$. Note: variations of the activity in the dark can be attributed to the use of biological samples. Note: *k* and LRF values are given as mean ± S.E.M. summarizing the individual values of all replicates.

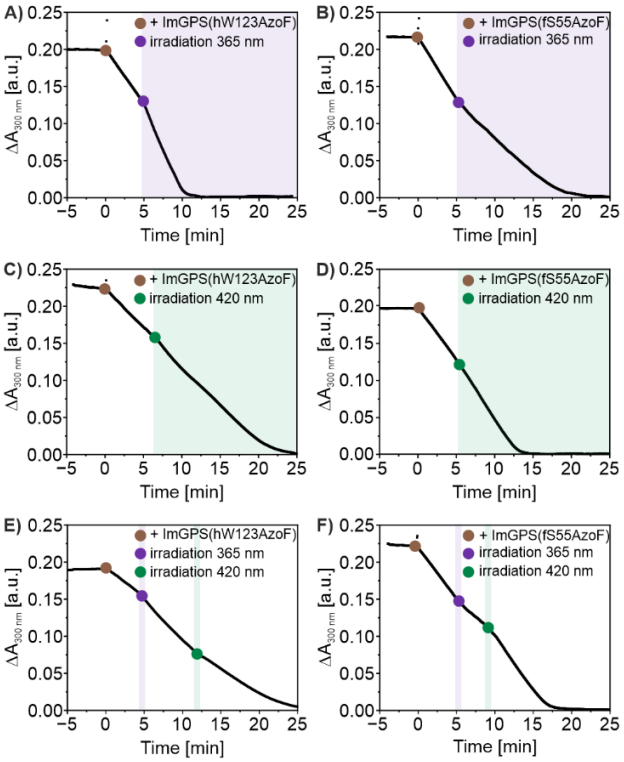

Figure 6. Comparison of ImGPS activity changes facilitated either by moderate (A,B) and low (C,D) VET or *E*↔*Z* switching of AzoF (E,F). Brown dot: reaction start at which ImGPS(hW123AzoF) (A, C, E) or ImGPS(fS55AzoF) (B, D, F) were added. Violet dot: start of 365 nm pulsed (A–D) or constantly powered (E,F) irradiation. Green dot: start of 420 nm pulsed (A–D) or constantly powered (E,F) irradiation. For reaction conditions see **Table 3**.

We started our investigation with injection of moderate and low VET via monochromatic pulsed irradiation. For 365 nm, we obtained a ~1.9-fold activity increase for ImGPS(hW123AzoF) and a ~1.7-fold activity decrease for ImGPS(fS55AzoF) (**Figure 6A,B**; **Table 3**). In comparison, enzyme activity was unaffected by irradiation with 420 nm with LRFs of ~1.0 for ImGPS(hW123AzoF) and ~1.2 for ImGPS(fS55AzoF) (**Figure 6C,D; Table 3**). While the observed activity increase for ImGPS(hW123AzoF) upon 365 nm irradiation matched our ambition to promote catalysis via VET, it clearly coincided with our previous result (LRF ~1.9) that we acquired by irradiating the enzyme prior to the measurement with light of 365 nm (**Table 2**).[29] The same was true for ImGPS(fS55AzoF), for which we also observed an activity decrease (LRF ~2.3) in our previous study.[30] We therefore reasoned that the effects of ImGPS(hW123AzoF) and ImGPS(fS55AzoF) that were caused during monochromatic irradiation were mainly due to the configurational change of AzoF. To confirm this, we used an experimental setup, in which we initiated the reaction by addition of the enzyme, followed PRFAR turnover for ~5 min in the dark, then irradiated the reaction with 365 nm for ~30 s to obtain PSS_Z^{365nm}, followed the reaction progress again in the dark for another ~5 min, then irradiated the reaction with 420 nm for ~30 s to obtain PSS_E^{420nm}, and followed the reaction in the dark until it was completed (**Figure 6E,F**). The activity of ImGPS(hW123AzoF) was increased in PSS_Z^{365nm} (LRF ~1.6; **Table 3**) and returned to initial values in PSS_E^{420nm} (LRF ~1.8). Likewise, the activity of ImGPS(fS55AzoF) was reduced in PSS_Z^{365nm} (LRF ~1.5) and again returned to initial values in PSS_E^{420nm} (LRF ~1.6). These results were consistent with the values measured during continuous monochromatic irradiation. Hence, we concluded that VET injection was either too low or the effects could not be separated from the effects that were induced by the *E*↔*Z* switching of AzoF.

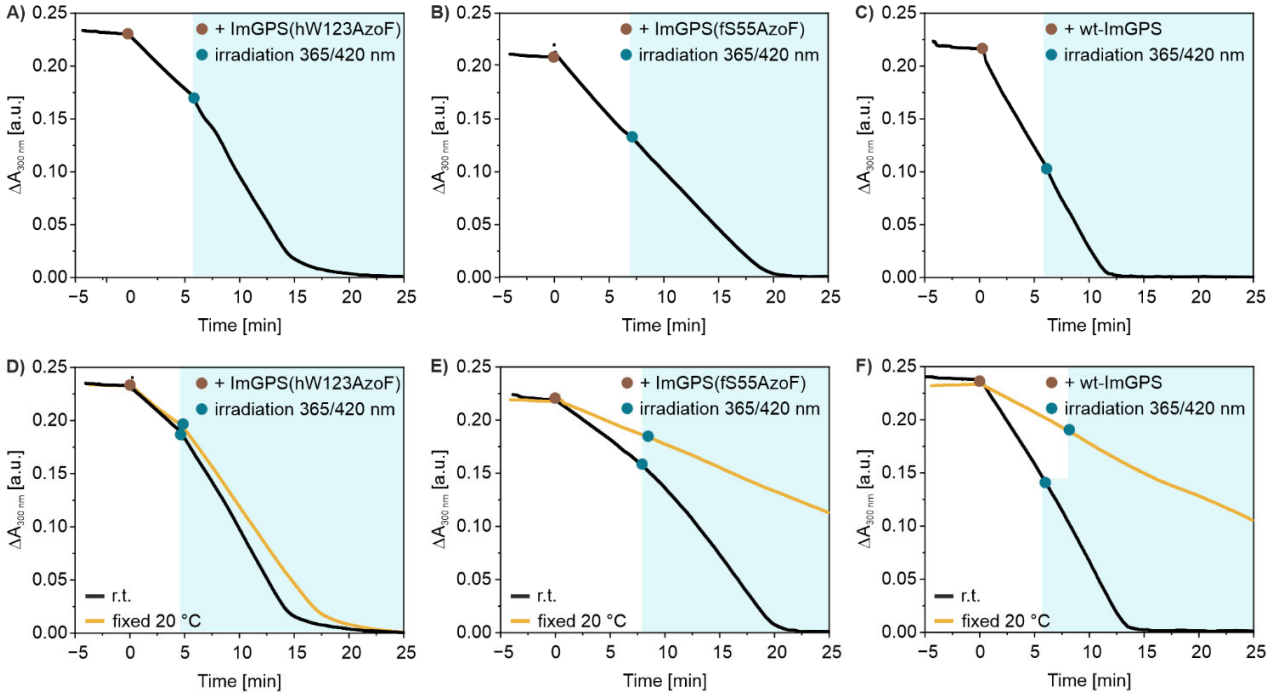

Figure 7. Comparison of ImGPS activity changes facilitated by high VET in ImGPS(hW123AzoF) (A,D), ImGPS(fS55AzoF) (B,E) and wt-ImGPS (C,F). The reactions were either irradiated with dichromatic pulsed (A–C; 1000 Hz) or constantly powered (D–F) irradiation at room temperature (r.t.; black) or with fixed temperature control at 20°C (yellow). Brown dot: reaction start at which enzyme was added. Cyan dot: start of irradiation. For reaction conditions see **Table 4**.

ImGPS activity control via high VET

Next, we measured the effects of dichromatic pulsed irradiation on ImGPS activity with the same experimental setup as described above (**Figure 7A–C**). Similar to the UV/Vis analyses, we started by testing different frequencies of 1–1000 Hz for ImGPS(hW123AzoF), ImGPS(fS55AzoF) as well as wt-ImGPS as a control. The effect of irradiation for each respective variant was the same for all pulsing frequencies. Hence, we summarized the activity and LRF values for all replicates of each variant ("total" in **Table 4**). As a result, we obtained an activity increase for ImGPS(hW123AzoF) with an LRF of ~1.6. Remarkably, ImGPS(fS55AzoF) and wt-ImGPS remained mainly unaffected by the dichromatic irradiation with LRFs of ~1.1 and ~1.0, respectively. This finding contrasts with monochromatic irradiation, by which enzyme activity was affected in ImGPS(hW123AzoF) and ImGPS(fS55AzoF) (**Figure 6**; **Table 3**). For this reason, we considered that the activity increase of ImGPS(hW123AzoF) during dichromatic irradiation might be caused by VET and performed further experiments to better assess this result.

First, we were interested whether we could reproduce the behavior of all three variants with dichromatic constantly powered irradiation. Surprisingly, by using the same experimental setup at room temperature, we observed an activity increase not only in ImGPS(hW123AzoF) with an LRF of ~1.8 but also in ImGPS(fS55AzoF) and wt-ImGPS with LRFs of ~1.4 and ~1.2, respectively (**Figure 7D–F, black; Table 4**). We contemplated that this discrepancy might be caused by a temperature increase of the sample owing to the technical alteration of irradiation using constant current (cf. **SI part1: Figure S7**). To counteract, we repeated our measurements with temperature control set to 20°C. Accordingly, the absolute activity values were smaller in comparison to room temperature (**Figure 7D–F, yellow;** Table 1); however, ImGPS(hW123AzoF) again responded with an activity increase of ~1.5, whereas ImGPS(fS55AzoF) and wt-ImGPS were nearly unaffected with LRFs of ~1.1 and ~1.0, respectively. These results supported our initial assumption that the LRF in ImGPS(hW123AzoF) is caused by VET. Moreover, it appears that the effect is independent of the technical implementation of irradiation whereby pulsed irradiation is the preferred technical implementation since it did not lead to an activity increase in wt-ImGPS. We conclude that pulsed irradiation does not produce as much heat as constantly powered irradiation, which makes it more appropriate for biological experiments.

The 1–3% activity decrease during dichromatic irradiation of wt-ImGPS (**Table 4**) is below the 5% significance level and might be caused by a slight depletion of PRFAR due to its light-sensitivity. In contrast, the 5–11% activity decrease of ImGPS(fS55AzoF) lies above this level and might be associated with the marginal isomerization of AzoF to its *Z* isomer (~35%) in $PSS1_E^{365/420nm}$. As shown for monochromatic 365 nm irradiation, isomerization to *Z* reduces activity in ImGPS(fS55AzoF). Consequently, the activity increase in ImGPS(hW123AzoF) might in part be caused by the configurational change of AzoF, as well. To test this hypothesis, we performed a new set of measurements with ImGPS(hW123AzoF), in which we limited the pulsed dichromatic irradiation to 3 min and subsequently followed the reaction progress in the dark until it was completed. If the activity increase was due to the configurational change of AzoF, it would remain after the irradiation stops (cf. **Figure 6E,F**). Remarkably, HisH activity returned to the initial low activity after the irradiation-facilitated increase with an LRF of ~2.0 (**Figure 8**; **Table 4**). This result suggests that the observed effect in ImGPS(hW123AzoF) is mainly caused by VET. However, we cannot exclude a small contribution of the configurational change of AzoF to the LRF.

Table 1. ImGPS activities subjected to dichromatic irradiation.

Variant	Pulse frequency	$k_{cat,app}$(*dark*) [min^{-1}]	$k_{cat,app}$(*during hν*) [min^{-1}]	$k_{cat,app}$(*after hν*) [min^{-1}]	LRF[a]	Replicates
Pulsed irradiation at room temperature[b]						
ImGPS(hW123AzoF)	1 Hz	20.6 ± 3.0	31.7 ± 5.0	—	1.54 ± 0.15 ↑	4
	10 Hz	19.6 ± 1.8	30.7 ± 3.0	—	1.57 ± 0.14 ↑	4
	100 Hz	22.9 ± 2.8	37.8 ± 6.0	—	1.63 ± 0.24 ↑	5
	1000 Hz	24.4 ± 2.0	38.2 ± 3.5	—	1.57 ± 0.16 ↑	10
	total	**21.1 ± 1.4**	**33.6 ± 2.6**	**—**	**1.59 ± 0.05 ↑**	**23**
ImGPS(fS55AzoF)	1 Hz	7.8 ± 1.0	7.9 ± 1.3	—	1.02 ± 0.10 ↓	5
	10 Hz	10.1 ± 0.9	9.2 ± 1.2	—	1.11 ± 0.11 ↓	4
	100 Hz	8.6 ± 1.3	8.1 ± 1.2	—	1.07 ± 0.05 ↓	6
	1000 Hz	11.3 ± 1.2	11.3 ± 1.6	—	1.04 ± 0.08 ↓	7
	total	**8.7 ± 0.7**	**8.4 ± 0.7**	**—**	**1.05 ± 0.03 ↓**	**22**
wt-ImGPS	1 Hz	53.5 ± 5.1	55.3 ± 7.2	—	1.03 ± 0.05 ↑	3
	10 Hz	55.2 ± 8.4	52.3 ± 1.8	—	1.05 ± 0.12 ↓	2
	100 Hz	65.5 ± 3.3	63.4 ± 10.6	—	1.05 ± 0.12 ↓	2
	1000 Hz	63.5 ± 5.7	61.2 ± 6.0	—	1.05 ± 0.05 ↓	7
	total	**60.4 ± 3.3**	**59.0 ± 3.5**	**—**	**1.03 ± 0.03 ↓**	**14**
Constantly powered irradiation at room temperature[b]						
ImGPS(hW123AzoF)	—	18.1 ± 1.9	32.6 ± 3.7	—	1.80 ± 0.11 ↑	5
ImGPS(fS55AzoF)	—	10.0 ± 4.2	13.9 ± 6.4	—	1.38 ± 0.23 ↑	3
wt-ImGPS	—	50.9 ± 5.6	60.4 ± 4.6	—	1.20 ± 0.07 ↑	3
Constantly powered irradiation at 20°C[c]						
ImGPS(hW123AzoF)	—	13.4 ± 0.6	20.3 ± 3.5	—	1.50 ± 0.23 ↑	5
ImGPS(fS55AzoF)	—	3.9 ± 0.3	3.6 ± 0.4	—	1.11 ± 0.08 ↓	5
wt-ImGPS	—	22.9 ± 2.3	23.1 ± 1.7	—	1.02 ± 0.03 ↑	5
3 min pulsed irradiation and recovery in the dark						
ImGPS(hW123AzoF)	1000 Hz	23.4 ± 0.8	46.8 ± 3.1		2.00 ± 0.26 ↑	6
			46.8 ± 3.1	23.5 ± 1.6	2.04 ± 0.48 ↓	

ImGPS activity: 50 mM Tris-acetate (pH 7.5), 0.6 μM HisA (to convert ProFAR to PRFAR), ~40 μM (saturated) ProFAR, 10 mM (saturated) glutamine, and 0.025–0.2 mM ImGPS. [a] The activity change is indicated by an upwards (activity increase) or downwards arrow (activity decrease). [b] Not subjected to temperature control. [c] Subjected to temperature control. Note: variations of the activity in the dark can be attributed to the use of biological samples. Note: *k* and LRF values are given as mean ± S.E.M. summarizing the individual values of all replicates.

Evaluation of the intensity and site requirements for VET to promote enzyme activity

Following up on the last set of experiments, which implicated that the activity increase of ImGPS(hW123AzoF) during dichromatic irradiation was induced by VET, we intended to draw some conclusions for the implementation of our concept. To this end, we focused on two key factors that are paramount to successfully influence enzyme activity by VET: i) the size of the local energy input, and ii) the requirements on the site of AzoF incorporation.

We first set out to get an approximation of the size of energy that reached the HisH active site and mediated the acceleration of catalysis. For this, we compared the increase in activity achieved by VET (local energy input) to the one obtained by a raise in temperature (global energy input) by measuring $k_{cat,app}$ at 4°C, 20°C, 30°C and 40°C for ImGPS(hW123AzoF) in its as-isolated form. Plotting the logarithm of $k_{cat,app}$ against the temperature allowed us to evaluate that a raise in temperature of ΔT ~5.7–8.4 K led to the same activity increase of 1.6–2.0 as was determined for VET in ImGPS(hW123AzoF) (**SI part1: Figure S21**)

By multiplying ΔT with the universal gas constant R = 8.314 J mol^{-1} K^{-1}, we obtained an estimation of the energy that helped overcome the catalytic energy barrier in HisH of VE_{cat} ~ 0.20–0.29 kcal mol^{-1}. In comparison, *E* azobenzene gains 52–64 kcal mol^{-1} with S0→S1 excitation, and 86–93 kcal mol^{-1} with S0→S2 excitation.[48–52] Hence, VE_{cat} represents only a tiny fraction (<1%) of the total VE

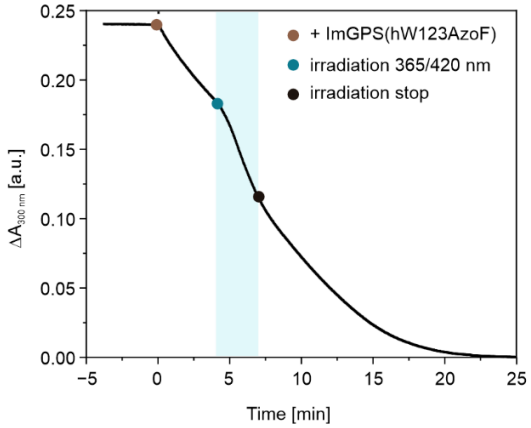

Figure 1. Recovery of ImGPS activity after high VET. Brown dot. Reaction start at which ImGPS(hW123AzoF) was added. Cyan dot: start of dichromatic pulsed (1000 Hz) irradiation. Black dot: stop of irradiation. For reaction conditions see Table 1.

that was injected, which is plausible since VE disperses without direction and declines with the covered distance after injection into the protein. Since VET is further reduced during monochromatic irradiation compared to dichromatic irradiation (cf. **Figure 4** and **Figure 5**), VE_{cat} produced by monochromatic irradiation is probably too low to initiate an activity change that can be detected in ImGPS(hW123AzoF). Due to this observation, we also suspect that other VET donors such as the azulene-based UAA AzAla[53,54] might not be able to promote ImGPS activity in position hW123, since they undergo only a single transition, in the case of AzAla S0→S1. It should, however, be considered that various other factors might influence the effectivity of VET to promote enzyme activity, such as the size of the catalytic activation barrier. For our studies, we chose the PRFAR-stimulated HisH reaction as it exhibits a lower energy barrier that might be overcome more easily by VET. However, following the law of Arrhenius the same amount of temperature energy ΔT obtains a higher activity increase in enzymes with a large energy barrier than in enzymes with a low energy barrier. It therefore remains to be determined, whether the influence of VET injection on enzyme activity follows the same rules as Arrhenius, or whether it behaves differently.

The conclusion that VE disperses without direction and declines with the distance from the injection point further substantiates the importance of the VET donor position in the enzyme. It means that VET only helps to overcome the energy barriers of conformational state interconversions close to the VET donor. However, VET will only promote enzyme activity if these interconversions are also relevant for catalysis. This argument is reinforced by the observation that dichromatic irradiation only caused an activity increase in ImGPS(hW123AzoF) but not in ImGPS(fS55AzoF). Apart from the differences in distance to the active site (~16 and ~33 Å, respectively), it appears that the >µs transitions close to hW123 have a stronger connection to catalytic turnover than the ≤µs dynamics close to fS55. Though one should keep this in mind for further VET experiments in ImGPS, it is difficult to generalize this observation for all enzymes. In other enzymes, catalysis might more strongly depend on ≤µs conformational interconversions than on >µs transitions and, hence, VET might be more effective in positions that contribute to ≤µs motions. Moreover, the mechanism by which the photo-induced switch of AzoF influences ImGPS activity in positions hW123 and fS55 is still uncertain. Activity will be influenced by either a change in the stability of conformational populations or a change of the energy barriers connected to the conformational interconversions. Both of these alterations induced by AzoF incorporation might affect VET-induced enzyme catalysis. In this regard, we also encountered difficulties in distinguishing between VET effects and E↔Z switching effects on activity during monochromatic irradiation. To differentiate between both effects, we therefore argue to choose incorporation positions in future studies, in which the configurational change of AzoF does not affect enzyme activity.

CONCLUSION

Enzymes are fascinating machineries with a complex interplay of conformation and catalysis. Fine-tuning of enzyme activity is realized by environmental factors that either cause the (de)stabilization of conformational states or the change of dynamics, meaning the interconversion rates between these states, on all timescales. While allostery alters the energy barriers to increase dynamics, a direct energy input, such as a rise in temperature, simply provides additional energy to overcome the barriers more rapidly. By using a light-sensitive unnatural amino acid, this energy input can be inserted with precise spatial control at any site within the enzyme and with faster temporal control than temperature.

For the proof-of-concept, we exploited the ability of the photoswitchable unnatural amino acid AzoF to inject vibrational energy into proteins, a process known as vibrational energy transfer (VET). Our studies thereby suggested that the site of AzoF incorporation was crucial and that high amounts of vibrational energy were required for the successful enhancement of enzyme activity. In particular, the site of incorporation should contribute to dynamics that are relevant for catalysis and should be located close to the active site. Remarkably, dichromatic irradiation, which was pivotal to inject a high amount of vibrational energy, generated an unknown AzoF species that might be involved in VET. Furthermore, we could unambiguously assign the observed increase in enzyme activity during irradiation to VET due to the recovery of enzyme activity in the dark. This success is primarily based on the use of imidazole glycerol phosphate synthase as a dynamic-driven enzyme system and the careful evaluation of positions for the incorporation of AzoF. Further studies on the influence of different VET donors, different energy barriers and different distances of incorporation to the active site will help develop this approach. Finally, this proof-of-concept paves the way for sophisticated investigations of the relations between dynamics and catalysis in enzyme systems.

ASSOCIATED CONTENT

Supporting Information part1 (PDF). This document includes the complete experimental section, additional figures associated with the introduction and an extended results section. We particularly included raw data on results that are provided in processed form in the main text such as time-resolved UV/Vis spectra and steady state kinetic measurements. Moreover, we included a full description of preliminary NMR experiments that are mentioned in the main text.

Supporting Information part2 (PDF). This document contains a full description of the MD simulation experiments and their evaluation using PCA. This material is available free of charge via the Internet at http://pubs.acs.org.

AUTHOR INFORMATION

Corresponding Author

* Dr. A. Hupfeld (née Kneuttinger)
Institute of Biophysics and Physical Biochemistry
Regensburg Center for Biochemistry
University of Regensburg
Universitätsstraße 31, D-93053 Regensburg (Germany)
E-mail: andrea.kneuttinger@ur.de

Present Addresses

† F. Zeqiri
Department of Biophysics
Ruhr University Bochum
Universitätsstraße 150, D-44780 Bochum (Germany)

Author Contributions

All authors have given approval to the final version of the manuscript.
‡ These authors contributed equally.

ACKNOWLEDGMENT

The authors thank Prof. Dr. Remco Sprangers and Prof. Dr. Reinhard Sterner for lively discussions on the topic, help with NMR measurements and proof-reading the manuscript. We also thank Dr. Enrico Hupfeld for his involvement in preliminary data acquisition, and Elias Wippermann and Karla Hernandez for support with the analysis of the MD simulations and OPLS force field parametrization. Most of all, we are grateful for the strong technical support team consisting of Julia Zach, Jeannette Ueckert and Achim Stark.

ABBREVIATIONS

AzoF, phenylalanine-4'-azobenzene
ImGPS, imidazole glycerol phosphate synthase
LED, light-emitting diode
MD, molecular dynamics
NMR, nuclear magnetic resonance
PCA, principal component analysis
PSS, photostationary state
SPM, shortest path map
VE, vibrational energy
VET, vibrational energy transfer
UV/Vis, ultraviolet to visible range of electromagnetic spectrum

REFERENCES

(1) Möglich, A.; Moffat, K. Engineered photoreceptors as novel optogenetic tools. *Photochem. Photobiol. Sci.* **2010**, *9* (10), 1286–1300. DOI: 10.1039/C0PP00167H.
(2) Ziegler, T.; Möglich, A. Photoreceptor engineering. *Front. Mol. Biosci.* **2015**, *2*, 30. DOI: 10.3389/fmolb.2015.00030.
(3) Mathony, J.; Niopek, D. Enlightening allostery:Designing switchable proteins by photoreceptor fusion. *Adv. Biol.* **2021**, *5* (5), 2000181. DOI: 10.1002/adbi.202000181.
(4) Pieper, J.; Buchsteiner, A.; Dencher, N. A.; Lechner, R. E.; Hauß, T. Light-induced modulation of protein dynamics during the photocycle of bacteriorhodopsin. *Photochem. Photobiol.* **2009**, *85* (2), 590–597. DOI: 10.1111/j.1751-1097.2008.00501.x.
(5) Strickland, D.; Yao, X.; Gawlak, G.; Rosen, M. K.; Gardner, K. H.; Sosnick, T. R. Rationally improving LOV domain–based photoswitches. *Nat. Methods* **2010**, *7* (8), 623–626. DOI: 10.1038/nmeth.1473.
(6) Henzler-Wildman, K.; Kern, D. Dynamic personalities of proteins. *Nature* **2007**, *450* (7172), 964–972. DOI: 10.1038/nature06522.
(7) Maria-Solano, M. A.; Serrano-Hervás, E.; Romero-Rivera, A.; Iglesias-Fernández, J.; Osuna, S. Role of conformational dynamics in the evolution of novel enzyme function. *Chem. Commun.* **2018**, *54* (50), 6622–6634. DOI: 10.1039/C8CC02426J.
(8) Rubtsova, N. I.; Rubtsov, I. V. Vibrational energy transport in molecules studied by relaxation-assisted two-dimensional infrared spectroscopy. *Annu. Rev. Phys. Chem.* **2015**, *66* (Volume 66, 2015), 717–738. DOI: 10.1146/annurev-physchem-040214-121337.
(9) Hamm, P.; Ohline, S. M.; Zinth, W. Vibrational cooling after ultrafast photoisomerization of azobenzene measured by femtosecond infrared spectroscopy. *J. Chem. Phys.* **1997**, *106* (2), 519–529. DOI: 10.1063/1.473392.
(10) Rubtsov, I. V.; Burin, A. L. Ballistic and diffusive vibrational energy transport in molecules. *J. Chem. Phys.* **2019**, *150* (2), 20901. DOI: 10.1063/1.5055670.
(11) Brown, C. J. A refinement of the crystal structure of azobenzene. *Acta Crystallogr.* **1966**, *21* (1), 146–152. DOI: 10.1107/S0365110X66002445.
(12) Crecca, C. R.; Roitberg, A. E. Theoretical study of the isomerization mechanism of azobenzene and disubstituted azobenzene derivatives. *J. Phys. Chem. A* **2006**, *110* (26), 8188–8203. DOI: 10.1021/jp057413c.
(13) Forber, C. L.; Kelusky, E. C.; Bunce, N. J.; Zerner, M. C. Electronic spectra of *cis*- and *trans*-azobenzenes: consequences of *ortho* substitution. *J. Am. Chem. Soc.* **1985**, *107* (21), 5884–5890. DOI: 10.1021/ja00307a009.
(14) Gagliardi, L.; Orlandi, G.; Bernardi, F.; Cembran, A.; Garavelli, M. A theoretical study of the lowest electronic states of azobenzene:The role of torsion coordinate in the *cis-trans* photoisomerization. *Theor. Chem. Acc.* **2004**, *111* (2), 363–372. DOI: 10.1007/s00214-003-0528-1.
(15) Mostad, A.; Rømming, C.; Hammarström, S.; Lousberg, R. J. J. C.; Weiss, U. A refinement of the crystal structure of *cis*-azobenzene. *Acta Chem. Scand.* **1971**, *25*, 3561–3568. DOI: 10.3891/acta.chem.scand.25-3561.
(16) Ladányi, V.; Dvořák, P.; Al Anshori, J.; Vetráková, L.; Wirz, J.; Heger, D. Azobenzene photoisomerization quantum yields in methanol redetermined. *Photochem. Photobiol. Sci.* **2017**, *16* (12), 1757–1761. DOI: 10.1039/c7pp00315c.
(17) Bandara, H. M. D.; Burdette, S. C. Photoisomerization in different classes of azobenzene. *Chem. Soc. Rev.* **2012**, *41* (5), 1809–1825. DOI: 10.1039/C1CS15179G.
(18) Casellas, J.; Bearpark, M. J.; Reguero, M. Excited-state decay in the photoisomerisation of azobenzene:A new balance between mechanisms. *ChemPhysChem* **2016**, *17* (19), 3068–3079. DOI: 10.1002/cphc.201600502.
(19) Bose, M.; Groff, D.; Xie, J.; Brustad, E.; Schultz, P. G. The incorporation of a photoisomerizable amino acid into proteins in *E. coli*. *J. Am. Chem. Soc.* **2006**, *128* (2), 388–389. DOI: 10.1021/ja055467u.
(20) Rivalta, I.; Sultan, M. M.; Lee, N.-S.; Manley, G. A.; Loria, J. P.; Batista, V. S. Allosteric pathways in imidazole glycerol phosphate synthase. *Proc. Natl. Acad. Sci. U. S. A.* **2012**, *109* (22), E1428. DOI: 10.1073/pnas.1120536109.
(21) Negre, C. F. A.; Morzan, U. N.; Hendrickson, H. P.; Pal, R.; Lisi, G. P.; Loria, J. P.; Rivalta, I.; Ho, J.; Batista, V. S. Eigenvector centrality for characterization of protein allosteric pathways. *Proc. Natl. Acad. Sci. U. S. A.* **2018**, *115* (52), E12201–E12208. DOI: 10.1073/pnas.1810452115.
(22) Maschietto, F.; Gheeraert, A.; Piazzi, A.; Batista, V. S.; Rivalta, I. Distinct allosteric pathways in imidazole glycerol phosphate synthase from yeast and bacteria. *Biophys. J.* **2022**, *121* (1), 119–130. DOI: 10.1016/j.bpj.2021.11.2888.
(23) Maschietto, F.; Morzan, U. N.; Tofoleanu, F.; Gheeraert, A.; Chaudhuri, A.; Kyro, G. W.; Nekrasov, P.; Brooks, B.; Loria, J. P.; Rivalta, I.; Batista, V. S. Turning up the heat mimics allosteric signaling in imidazole-glycerol phosphate synthase. *Nat. Commun.* **2023**, *14* (1), 2239. DOI: 10.1038/s41467-023-37956-1.
(24) Wurm, J. P.; Sung, S.; Kneuttinger, A. C.; Hupfeld, E.; Sterner, R.; Wilmanns, M.; Sprangers, R. Molecular basis for the allosteric activation mechanism of the heterodimeric imidazole glycerol phosphate synthase

complex. *Nat. Commun.* **2021**, *12* (1), 2748. DOI: 10.1038/s41467-021-22968-6.
(25) Calvó-Tusell, C.; Maria-Solano, M. A.; Osuna, S.; Feixas, F. Time evolution of the millisecond allosteric activation of imidazole glycerol phosphate synthase. *J. Am. Chem. Soc.* **2022**, *144* (16), 7146–7159. DOI: 10.1021/jacs.1c12629.
(26) Hiefinger, C.; Mandl, S.; Wieland, M.; Kneuttinger, A. Chapter Eight:Rational design, production and in vitro analysis of photoxenoproteins. In *Integrated methods in protein biochemistry: part C*; Shukla, A. K., Ed.; Methods in Enzymology; Academic Press, 2023; pp 247–288. DOI: 10.1016/bs.mie.2022.12.003.
(27) Liu, C. C.; Schultz, P. G. Adding new chemistries to the genetic code. *Annu. Rev. Biochem.* **2010**, *79* (1), 413–444. DOI: 10.1146/annurev.biochem.052308.105824.
(28) Kneuttinger, A. C. A guide to designing photocontrol in proteins:Methods, strategies and applications. *Biol. Chem.* **2022**, *403* (5-6), 573–613. DOI: 10.1515/hsz-2021-0417.
(29) Kneuttinger, A. C.; Rajendran, C.; Simeth, N. A.; Bruckmann, A.; König, B.; Sterner, R. Significance of the protein interface configuration for allostery in imidazole glycerol phosphate synthase. *Biochemistry* **2020**, *59* (29), 2729–2742. DOI: 10.1021/acs.biochem.0c00332.
(30) Kneuttinger, A. C.; Straub, K.; Bittner, P.; Simeth, N. A.; Bruckmann, A.; Busch, F.; Rajendran, C.; Hupfeld, E.; Wysocki, V. H.; Horinek, D.; König, B.; Merkl, R.; Sterner, R. Light regulation of enzyme allostery through photo-responsive unnatural amino acids. *Cell Chem. Biol.* **2019**, *26* (11), 1501–1514. DOI: 10.1016/j.chembiol.2019.08.006.
(31) Douangamath, A.; Walker, M.; Beismann-Driemeyer, S.; Vega-Fernandez, M.; Sterner, R.; Wilmanns, M. Structural evidence for ammonia tunneling across the $(\beta\alpha)_8$ barrel of the imidazole glycerol phosphate synthase bienzyme complex. *Structure* **2002**, *10* (2), 185–193. DOI: 10.1016/S0969-2126(02)00702-5.
(32) Beismann-Driemeyer, S.; Sterner, R. Imidazole glycerol phosphate synthase from *Thermotoga maritima*:Quaternary structure, steady-state kinetics, and reaction mechanism of the bienzyme complex. *J. Biol. Chem.* **2001**, *276* (23), 20387–20396. DOI: 10.1074/jbc.M102012200.
(33) List, F.; Vega, M. C.; Razeto, A.; Häger, M. C.; Sterner, R.; Wilmanns, M. Catalysis uncoupling in a glutamine amidotransferase bienzyme by unblocking the glutaminase active site. *Chem. Biol.* **2012**, *19* (12), 1589–1599. DOI: 10.1016/j.chembiol.2012.10.012.
(34) Lisi, G. P.; Manley, G. A.; Hendrickson, H.; Rivalta, I.; Batista, V. S.; Loria, J. P. Dissecting dynamic allosteric pathways using chemically related small-molecule activators. *Structure* **2016**, *24* (7), 1155–1166. DOI: 10.1016/j.str.2016.04.010.
(35) Lisi, G. P.; Currier, A. A.; Loria, J. P. Glutamine hydrolysis by imidazole glycerol phosphate synthase displays temperature dependent allosteric activation. *Front. Mol. Biosci.* **2018**, *5*, 4. DOI: 10.3389/fmolb.2018.00004.
(36) Klem, H.; Alegre-Requena, J. V.; Paton, R. S. Catalytic effects of active site conformational change in the allosteric activation of imidazole glycerol phosphate synthase. *ACS Catal.* **2023**, *13* (24), 16249–16257. DOI: 10.1021/acscatal.3c04176.
(37) Stadler, E.; Eibel, A.; Fast, D.; Freißmuth, H.; Holly, C.; Wiech, M.; Moszner, N.; Gescheidt, G. A versatile method for the determination of photochemical quantum yields via online UV-Vis spectroscopy. *Photochem. Photobiol. Sci.* **2018**, *17* (5), 660–669. DOI: 10.1039/C7PP00401J.
(38) Rustler, K.; Nitschke, P.; Zahnbrecher, S.; Zach, J.; Crespi, S.; König, B. Photochromic evaluation of 3(5)-arylazo-1H-pyrazoles. *J. Org. Chem.* **2020**, *85* (6), 4079–4088. DOI: 10.1021/acs.joc.9b03097.
(39) Simeth, N. A.; Kinateder, T.; Rajendran, C.; Nazet, J.; Merkl, R.; Sterner, R.; König, B.; Kneuttinger, A. C. Towards photochromic azobenzene-based inhibitors for tryptophan synthase. *Chem. Eur. J.* **2021**, *27* (7), 2439–2451. DOI: 10.1002/chem.202004061.
(40) Calbo, J.; Weston, C. E.; White, A. J. P.; Rzepa, H. S.; Contreras-García, J.; Fuchter, M. J. Tuning azoheteroarene photoswitch performance through heteroaryl design. *J. Am. Chem. Soc.* **2017**, *139* (3), 1261–1274. DOI: 10.1021/jacs.6b11626.
(41) Luo, J.; Samanta, S.; Convertino, M.; Dokholyan, N. V.; Deiters, A. Reversible and tunable photoswitching of protein function through genetic encoding of azobenzene amino acids in mammalian cells. *ChemBioChem* **2018**, *19* (20), 2178–2185. DOI: 10.1002/cbic.201800226.
(42) Butler, W. L.; Hendricks, S. B.; Siegelman, H. W. Action spectra of phytochrome in vitro. *Photochem. Photobiol.* **1964**, *3* (4), 521–528. DOI: 10.1111/j.1751-1097.1964.tb08171.x.
(43) Fregoni, J.; Granucci, G.; Persico, M.; Corni, S. Strong coupling with light enhances the photoisomerization quantum yield of azobenzene. *Chem* **2020**, *6* (1), 250–265. DOI: 10.1016/j.chempr.2019.11.001.
(44) Cembran, A.; Bernardi, F.; Garavelli, M.; Gagliardi, L.; Orlandi, G. On the mechanism of the *cis–trans* isomerization in the lowest electronic states of azobenzene: S0, S1, and T1. *J. Am. Chem. Soc.* **2004**, *126* (10), 3234–3243. DOI: 10.1021/ja038327y.
(45) Merritt, I. C. D.; Jacquemin, D.; Vacher, M. *cis → trans* photoisomerisation of azobenzene:A fresh theoretical look. *Phys. Chem. Chem. Phys.* **2021**, *23* (35), 19155–19165. DOI: 10.1039/D1CP01873F.
(46) Takeshita, T.; Hara, M. Photoionization and *trans*-to-*cis* isomerization of β-cyclodextrin-encapsulated azobenzene induced by two-color two-laser-pulse excitation. *Spectrochim. Acta, Part A* **2018**, *193*, 475–479. DOI: 10.1016/j.saa.2017.12.061.
(47) Feldmeier, C.; Bartling, H.; Riedle, E.; Gschwind, R. M. LED based NMR illumination device for mechanistic studies on photochemical reactions – Versatile and simple, yet surprisingly powerful. *J. Magn. Reson.* **2013**, *232*, 39–44. DOI: 10.1016/j.jmr.2013.04.011.
(48) Tan, E. M. M.; Amirjalayer, S.; Smolarek, S.; Vdovin, A.; Zerbetto, F.; Buma, W. J. Fast photodynamics of azobenzene probed by scanning excited-state potential energy surfaces using slow spectroscopy. *Nat. Commun.* **2015**, *6* (1), 5860. DOI: 10.1038/ncomms6860.
(49) Griffiths, J. II. Photochemistry of azobenzene and its derivatives. *Chem. Soc. Rev.* **1972**, *1* (4), 481–493. DOI: 10.1039/CS9720100481.
(50) Bortolus, P.; Monti, S. *Cis-trans* photoisomerization of azobenzene. Solvent and triplet donor effects. *J. Phys. Chem.* **1979**, *83* (6), 648–652. DOI: 10.1021/j100469a002.
(51) Lednev, I. K.; Ye, T.-Q.; Abbott, L. C.; Hester, R. E.; Moore, J. N. Photoisomerization of a capped azobenzene in solution probed by ultrafast time-resolved electronic absorption spectroscopy. *J. Phys. Chem. A* **1998**, *102* (46), 9161–9166. DOI: 10.1021/jp982368c.
(52) Fujino, T.; Tahara, T. Picosecond time-resolved raman study of *trans*-azobenzene. *J. Phys. Chem. A* **2000**, *104* (18), 4203–4210. DOI: 10.1021/jp992757m.
(53) Baumann, T.; Hauf, M.; Schildhauer, F.; Eberl, K. B.; Durkin, P. M.; Deniz, E.; Löffler, J. G.; Acevedo-Rocha, C. G.; Jaric, J.; Martins, B. M.; Dobbek, H.; Bredenbeck, J.; Budisa, N. Site-resolved observation of vibrational energy transfer using a genetically encoded ultrafast heater. *Angew. Chem., Int. Ed.* **2019**, *58* (9), 2899–2903. DOI: 10.1002/anie.201812995.
(54) Löffler, J. G.; Deniz, E.; Feid, C.; Franz, V. G.; Bredenbeck, J. Versatile vibrational energy sensors for proteins. *Angew. Chem., Int. Ed.* **2022**, *61* (21), e202200648. DOI: 10.1002/anie.202200648.

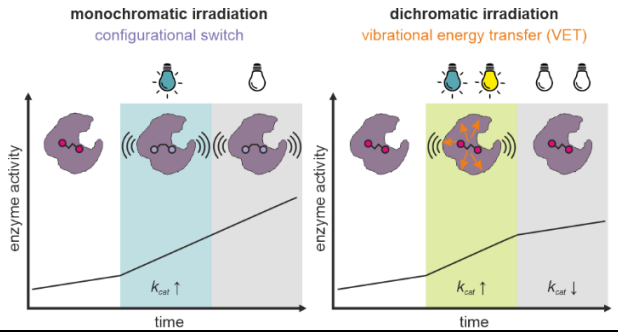
monochromatic irradiation
configurational switch
dichromatic irradiation
vibrational energy transfer (VET)
enzyme activity
time
k_{cat} ↑
enzyme activity
time
k_{cat} ↑
k_{cat} ↓